Discover Applied Sciences

Research

Study on the material removal mechanism and the exit breakage of ultrasonic vibration-assisted grinding for microcrystalline glass

Wenchao Zhang[1] · Enming Cui[1] · Baoquan Zhang[2] · Mingwei Wang[1] · Xiujun Zhao[1]

© The Author(s) 2024   OPEN

Abstract

With the aim of solving problems such as exit breakage and surface microcracks during microcrystalline glass machining, an ellipsoidal erosion model is established by analyzing the motion trajectory and characteristics of single diamond grit in ultrasonic vibration-assisted grinding (UVAG), and the material removal volume of single diamond grit particles is obtained. A simulation model of UVAG of microcrystalline glass is established by the finite element method. The effect of process parameters such as rotational speed, grinding depth, feed rate on grinding force and workpiece edge stress has been investigated. The experiment of UVAG for microcrystalline glass is performed on a five-axis CNC machine with the same process parameters, and the surface morphology, surface roughness, and exit breakage sizes of microcrystalline glass are observed. The results show that with the increase in grinding depth, the average grinding force between the tool and the workpiece increases, and the proportion of material removal in a brittle fracture increases. As the rotational speed increases, the grinding force between the tool and the workpiece gradually decreases and results in an improvement in the surface quality of the workpiece. As the feed rate increases, the surface roughness increases by 16.76%, the width of the edge breakage increases by 109.19%, and the thickness of the edge breakage increases by 104.49%.

Article highlights

(1) Considering ultrasonic vibration, the trajectory and characteristics of a single diamond grit is analyzed and a model of ellipsoidal erosion is established. The material removal volume in the case of single diamond grit grinding is obtained.

(2) The removal mechanism of hard and brittle materials as well as the surface quality after machining are investigated and analyzed by comparing the grinding force and exit stress of the workpiece under various process parameters.

(3) The finite element simulation model of UVAG of microcrystalline glass is established based on the JH2 constitutive model, and the effect of process parameters on grinding force and exit stress is obtained. The three-dimensional force sensor is used to obtain grinding forces during machining. The surface morphology of workpiece is observed by SEM and measured by white-light interferometer. The reliability of the simulation model is verified by comparing the experimental results with the simulation results.

Keywords Microcrystalline glass · Process parameters · Grinding force · Surface quality · Exit breakage

---

✉ Xiujun Zhao, zhaoxjdlpu@163.com | [1]School of Mechanical Engineering and Automation, Dalian Polytechnic University, Dalian, China. [2]Beijing Jingdiao Group Co., Ltd., Beijing, China.

1 Introduction

Microcrystalline glass is a typical hard and brittle material that is used extensively in the aerospace, medical, biological, and aviation industries. It has high strength, resistance to high temperatures, and resistance to corrosion, among other qualities [1]. Grinding is the main machining method for microcrystalline glass [2]. However, due to its high hardness and brittleness, it is easy to fracture and cause exit breakage with conventional grinding (CG), which affects the quality and service life of the workpiece. As an economical and effective ceramic machining method, UVAG has been widely used, which takes the advantage of ultrasonic waves owing to its excellent characteristics of high frequency, high energy impact, as well as vibration in the grinding process [3]. Research has shown that UVAG can effectively improve the surface topography and exit breakage phenomenon [4].

In recent years, many scholars have launched a large number of research experiments on the grinding of brittle materials. Ding et al. [5] studied the effects of grinding parameters on both the grinding force and grinding surface roughness between UVAG and CG. The grinding force and the roughness of the ground surface were shown to be reduced by various degrees during UVAG compared to CG. Li et al. [6] performed a single-factor experiment and discovered that the grinding force exhibited an upward trend as the grinding depth, feed rate, and amplitude increase. Conversely, the grinding force decreased as the rotational speed increases. Baraheni et al. [7] reported that UVAG can improve material removal rates. Wang et al. [8] investigated the effects of UVAG and CG on C/SiC composites and analyzed the variation in grinding force through different machining methods and process parameters. The research results demonstrated that the application of ultrasonic vibration can effectively enhance the machinability of C/SiC materials by softening them. Chen et al. [9] investigated the process and mechanism of machining sapphire using UVAG technology. It was shown that the application of ultrasonic vibrations can effectively reduce the force exerted on the material, and the reduction ratio is direction-dependent.

At present, many scholars have carried out research on UVAG of hard and brittle materials, such as Zhang et al. [10], Guo et al. [11], but there are few studies on the exit stress and the mechanism of edge breakage in UVAG of microcrystalline glass by means of simulation and experiment under different process parameters. In the next section, an ellipsoidal erosion model is established by analyzing the motion trajectory and characteristics of a single diamond grit in UVAG. In Sect. 2, the simulation model of UVAG of hard and brittle materials with electroplated diamond tool is established by ABAQUS finite element software based on the JH2 constitutive. In Sect. 3, simulation results and study the grinding forces and exit stresses under various rotational speeds, grinding depths, and feed rates are analyzed. In Sect. 4, the surface quality and exit edge breakage after machining are analyzed, and the machined surface is observed by white-light interferometer, SEM and other equipments. The accuracy and reliability of the simulation model are verified by experimental results, which provides theoretical guidance for selecting production parameters in practical applications. In the last section, the results of the study are compared with results presented in relevant papers published recently by other authors.

2 Kinematic analysis of single-grit grinding with ultrasonic vibration

Ultrasonic vibration-assisted grinding is a machining method that combines ultrasonic vibration with conventional grinding [12]. After ultrasonic vibration is added, the motion characteristics of the tool and the diamond grits are also changed with respect to the workpiece. The direction of ultrasonic vibration includes axial, radial, and tangential motion [13]. In this paper, axial UVAG is used to machine hard and brittle materials. The principle of axial UVAG is shown in Fig. 1. The tool rotates at a specific angular speed and moves horizontally at a specific feed rate when grinding. At the same time, the tool vibrates along the axis at a frequency higher than 20 kHz and a fixed amplitude (0–10 µm) [14]. During the machining process, the tool rotates at high speed and the bottom diamond grits rotate and grind the workpiece. Meanwhile, the tool makes high-frequency reciprocating motion along the axial direction and impacts the workpiece with a tiny amplitude. Finally, the material is removed by the combination effects of both grinding and hammering impact of the diamond grits on the workpiece surface.

In the process of axial UVAG, the motion of a single diamond grit includes rotational motion around the central axis of the tool at a linear speed of v_s, translational motion along the tangential direction of the tool at a linear speed of v_w, and high-frequency vibration of frequency f with amplitude A along the axis of the tool.

Assuming that the tool moves along the x-axis the equation of motion for a single diamond grit in UVAG is as follows:

Fig. 1 Schematic diagram of ultrasonic vibration-assisted grinding
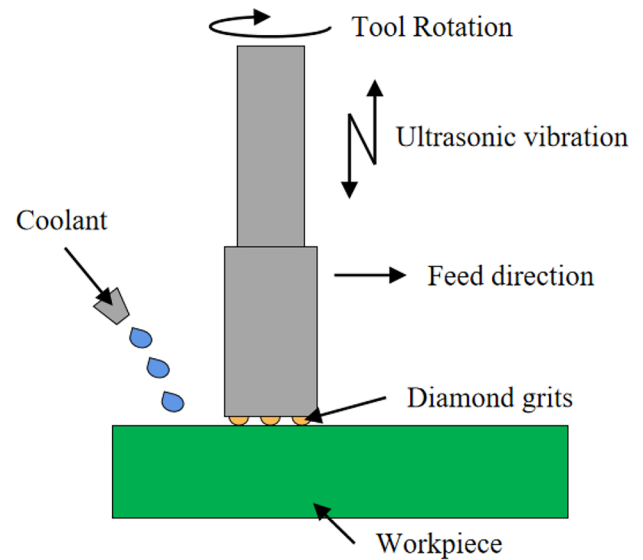
$$\begin{cases} X = R\cos(\omega_s t) + v_w t \\ Y = R\sin(\omega_s t) \\ Z = A\sin(\omega t + \phi) \end{cases} \tag{1}$$

where, ω_s is the angular speed of tool rotation, which is 10000r/min. R is the distance from the diamond grit to the axis of the tool, 2.5 mm. f is the frequency of the ultrasonic vibration, 20 kHz. ϕ is the initial phase of ultrasonic vibration, 0. t is time. and A is the amplitude, 3 μm.

The axial ultrasonic vibration-assisted grinding is used to apply regular and controllable high-frequency vibration to the tool in the axial direction, so as to change the motion law of the diamond grit on the tool and change the motion characteristics of the diamond grit during the grinding process. According to Eq. (1), the motion trajectory of a single diamond grit was simulated using MATLAB software and the motion trajectories in UVAG were obtained. And when $Z=0$, the trajectory is CG, as shown in Fig. 2a and b, respectively.

To study the volume of material removal by a single diamond grit, the model is simplified, and the assumptions are made as follows:

(1) The diamond grits on the bottom surface of the tool are evenly distributed.
(2) The workpiece material is isotropic.
(3) The amplitude and frequency of the ultrasound vibrations are constant during machining.
(4) The diamond grits are spherical and the shape remains unchanged during machining.

Figure 3 shows the diamond grit trajectory during a single cycle of UVAG. Assuming that the diamond grit begins to contact the workpiece surface at time m and separates at time n. In a cycle, the contact time of the tool and the workpiece is very short and the contact time Δt can be expressed as follows:

$$\Delta t = \frac{1}{\pi f}\left[\frac{\pi}{2} - \arcsin(1 - \frac{h}{A})\right] \tag{2}$$

where, h is the maximum grinding depth of the diamond grit.

In actual machining, the volume of material removal by a diamond grit can be approximated as ellipsoidal erosion, as shown in Fig. 4a.

As shown in Fig. 4b, an ellipsoid coordinate system is established with the center O as the origin. a is the axis of the ellipsoid, b is the semi-minor axis, and c is the polar axis distance. During grinding, the diamond grits begin to contact the workpiece at point F and separate at point G. PE is the maximum grinding depth and its length is h. The length of OP is c, and $c=r+A$ (r is the radius of the diamond grit). Since the radius of the diamond grit is much larger than the

Fig. 2 Motion trajectory for a single diamond grit
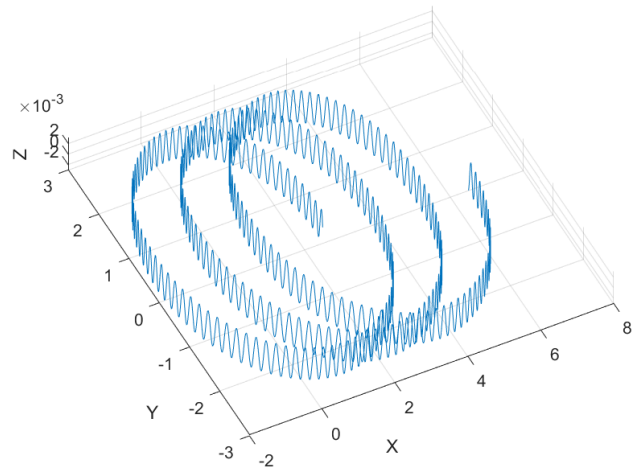
(a) Ultrasonic vibration-assisted grinding
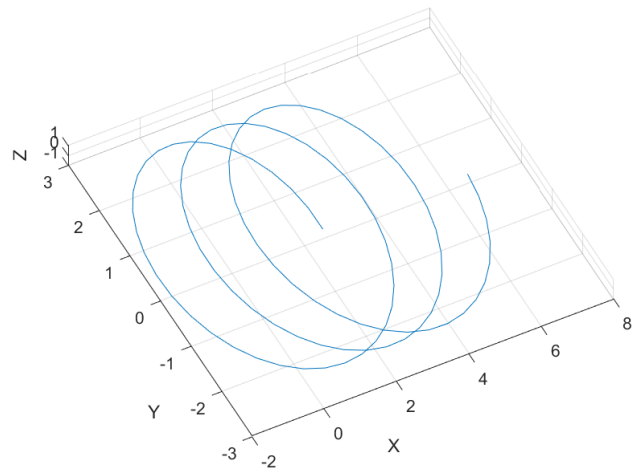
(b) Conventional grinding

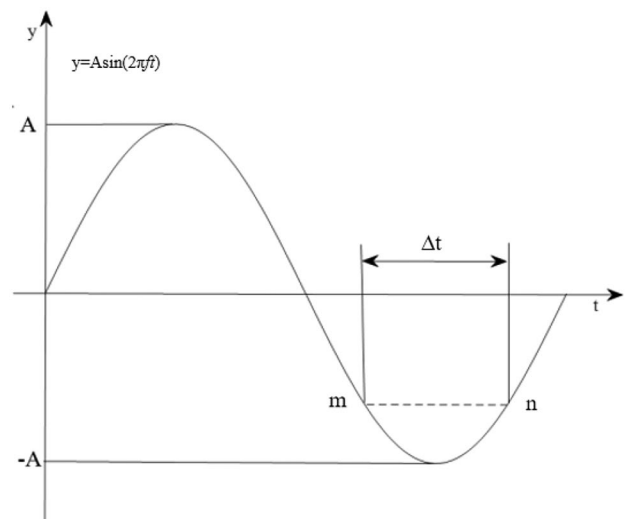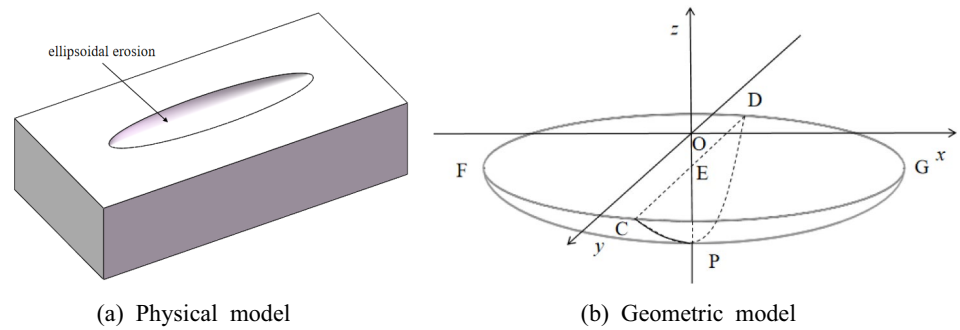**Fig. 3** The motion trajectory of the diamond grit in a single cycle

Fig. 4 The model of ellipsoidal erosion

(a) Physical model   (b) Geometric model

ultrasonic amplitude, c is approximately equal to r. The length of FG is the motion distance between the diamond grit and the workpiece in a single cycle. EC is the radius of the cross-section where the grit intersects the workpiece plane when the diamond grit moves to the lowest. The length of EC and FG can be expressed as follows:

$$l_{EC} = \sqrt{r^2 - (r-h)^2} = \sqrt{2rh - h^2} \tag{3}$$

$$l_{FG} = v\Delta t = \omega R\Delta t = 2n\pi R\Delta t \tag{4}$$

As the two points B and C are on the surface of the ellipsoid, the coordinates of the points G and C are ($n\pi R\Delta t$, 0, c-h) and ($0, \sqrt{2rh - h^2}, c$-h), respectively. The volume of material removal of a single diamond grit can be obtained in Eq. (7):

$$V = \frac{\pi^2 h^2 n R r \Delta t}{3\sqrt{2rh - h^2}} \left(3 - \frac{h}{r}\right) \tag{5}$$

3 Modelling of the grinding

Figure 5 is a finite element simulation model of UVAG of microcrystalline glass with the tool. Due to the complexity of tool modeling, the 3D modeling software was modeled and imported into the finite element simulation software. The diameter of the tool is 5 mm, and the abrasive particle size is 200 #. The model was simplified with 500 diamond grits overall, only being placed on the circular edge at the bottom of the tool, in order to increase computational efficiency. The microcrystalline glass is a cubic shape with dimensions of 3.0 mm×8.0 mm×0.3 mm. As a typical brittle and hard material, its material removal method is mainly brittle fracture. The simulation adopts the Johnson-Holmquist(JH2) constitutive model, which adopts the first strength theory to judge brittle fracture failure of ceramics [15, 16]. It is used to simulate the mechanical behaviors of brittle materials, such as strength, damage, and degradation under large deformation, high strain rate, and high pressure. The grids around the diamond grits are locally fined and the remaining areas are coarse. The approximate global size of the tool is 0.28 mm for seeding by seed part. The workpiece is seeding through the seed edge. The length is divided based on the double option in bias, with a minimum size of 0.03 mm and a maximum size of 0.06 mm. The width and height of the workpiece are seeded "by size", and its approximate element size is 0.04 mm. The tool element type adopts a 4-node linear tetrahedral grid and the microcrystalline glass adopts an 8-node linear hexahedral grid. The tool is defined as a rigid body, and the reference point RP is set at the center on the top of the tool.

Fig. 5 Finite element model of ultrasonic vibration-assisted grinding
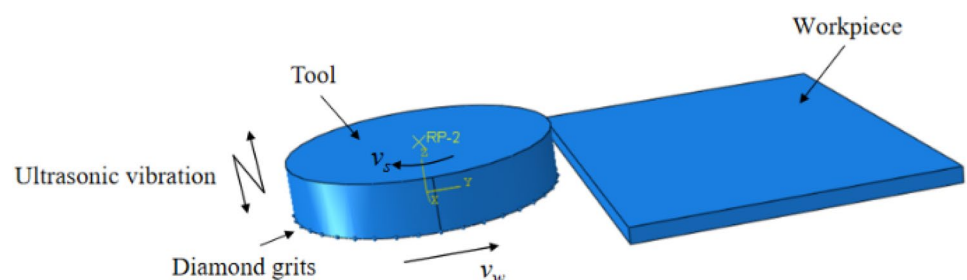
The contact method between the tool and the workpiece is surface-to-surface contact, and the tool is selected as the main surface and the workpiece is set as the slave surface. The boundary of the workpiece is "Symmetry/Antisymmetry/Encaster", where $U1 = U2 = U3 = UR1 = UR2 = UR3 = 0$. The boundary type of the tool is "Velocity/Angular velocity", and the parameters of feed rate and rotation speed are set. The tool moves in the positive direction of the y-axis and rotates clockwise. The tool simultaneously vibrates along the z-axis during the feed process.

According to the actual machining conditions, the process parameters adopted in the simulation are shown in Table 1. Among them, the rotational speeds are 10,000 r/min, 14,500 r/min, and 19,000 r/min. The grinding depths are 20 μm, 30 μm, and 40 μm. The feed rates are 1000 mm/min, 2000 mm/min, and 3000 mm/min. The ultrasonic frequency of all groups is 20 kHz and the ultrasonic amplitude is 3 μm. In a single-factor experiment, the effects of feed rate, grinding depth, and rotational speed on grinding force and exit stress have been studied. The material properties of microcrystalline glass and diamond grit are shown in Tables 2 and 3, respectively.

4 Simulation and analysis of ultrasonic vibration-assisted grinding

4.1 Analysis of the grinding force

4.1.1 Effect of feed rates on grinding force

Figure 6a, b, and c show the grinding force between the tool and the workpiece at different feed rates. As can be seen from Fig. 6, as the feed rate increases, the grinding force gradually increases, and the grinding force in the y direction changes the most. There is an increase in maximum force from 40 to 56 N. Figure 7 shows the curves of the average grinding force during the grinding at different feed rates. It can be seen from Fig. 7 that the average grinding forces in the x, y, and z directions increase with the feed rate. The reason for this is because a higher feed rate causes the diamond grit's

Table 1 Parameters of grinding

No	Rotational speed(r/min)	Grinding depth(μm)	Feed rate(mm/min)
1	10,000	20	1000
2	10,000	20	2000
3	10,000	20	3000
4	10,000	30	3000
5	10,000	40	3000
6	14,500	40	3000
7	19,000	40	3000

Table 2 Material parameters of microcrystalline glass

Property	Value
Density(kg/m^3)	2530
Shear Modulus(GPa)	25.5
Poisson's Ratio	0.29
Vickers Hardness(GPa)	6

Table 3 Material parameters of diamond grits

Property	Value
Density (kg/m^3)	3500
Young's Modulus(GPa)	964
Poisson's Ratio	0.2
Vickers Hardness(GPa)	78.5

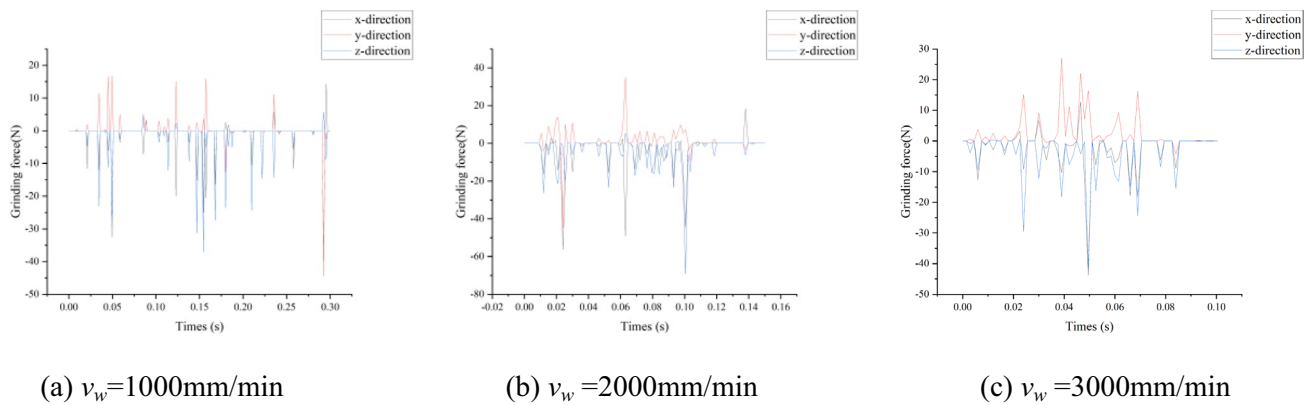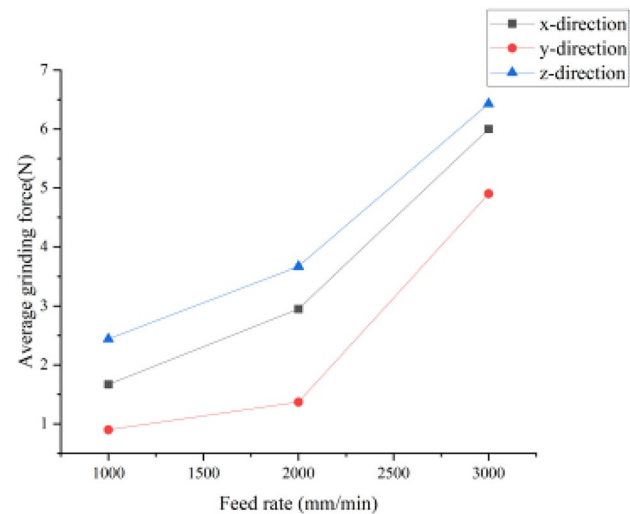(a) v_w=1000mm/min   (b) v_w =2000mm/min   (c) v_w =3000mm/min

Fig. 6 Grinding force at different feed rates

Fig. 7 Curves of the grinding force with feed rate

maximum cutting thickness to grow, which results in a significant amount of material removal. Therefore, the grinding force is also increased.

4.1.2 Effect of depths on the grinding force

Figure 8a, b, and c show the grinding force between the tool and the workpiece at different grinding depths. As can be seen from Fig. 8, as the grinding depth increases, the maximum grinding force in the y-direction increases from 56 to 170 N. The average grinding force curves at different grinding depths are displayed in Fig. 9. It can be seen from Fig. 9 that the grinding force in directions x, y, and z gradually increases with the grinding depth. Due to the increase in grinding depth, the number of diamond grits involved in grinding increases, which results in the increasement of both the volume of material removal and the load of the tool. Therefore, the grinding force rises.

4.1.3 Effect of rotational speeds on the grinding force

Figure 10a, b, and c show the grinding force between the tool and the workpiece at different rotational speeds. As can be seen from Fig. 10, the maximum grinding force in the y direction decreases from 170 to 80 N as the rotational speed rises. Figure 11 shows the curves of the average grinding force during the grinding at different rotational speeds. Figure 11 shows that when rotational speed increases, the grinding force in the x, y, and z directions decreases. The reason is mainly that the increase in rotational speed reduces the maximum length of the diamond grits that cut into the workpiece each time. The grinding times for each grit involved in grinding increases, and the effective contact time between the diamond grit and the workpiece decreases. Consequently, the grinding force reduces as the rotational speed increases.
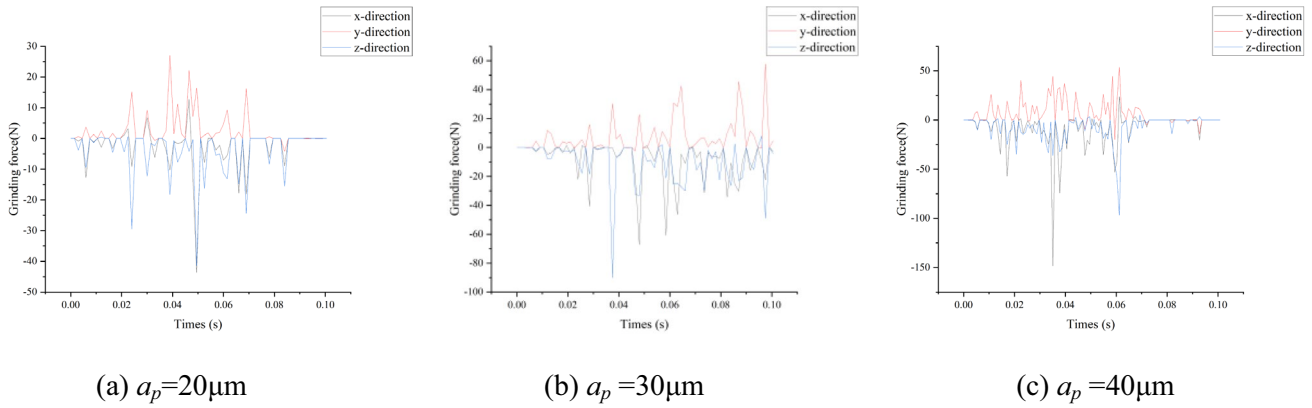
(a) a_p=20μm   (b) a_p =30μm   (c) a_p =40μm

Fig. 8 Grinding force at different depths

Fig. 9 Curves of the grinding force with depths

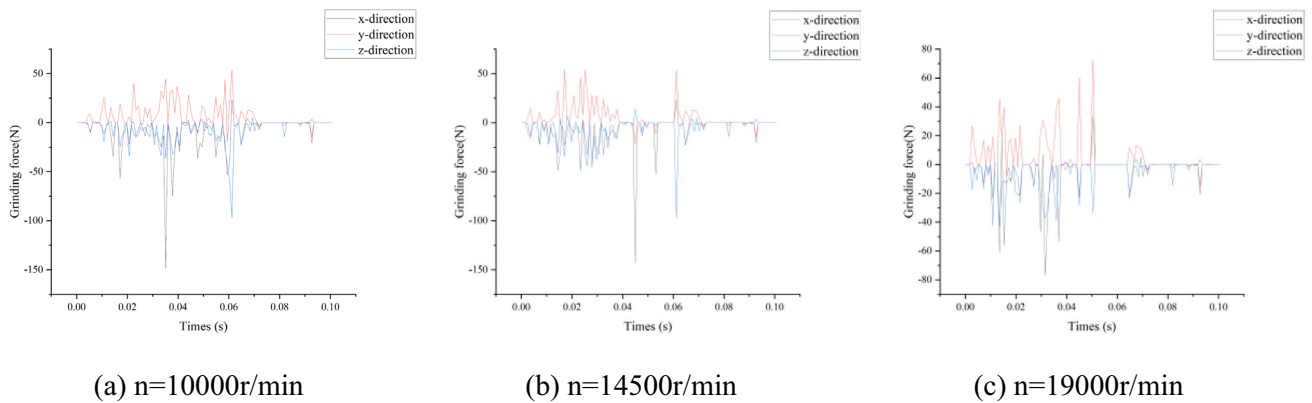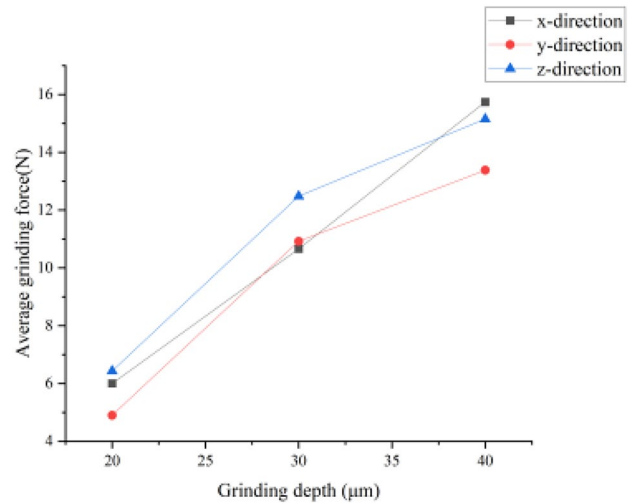(a) n=10000r/min   (b) n=14500r/min   (c) n=19000r/min

Fig. 10 Grinding force at different rotational speeds

4.2 Analysis of the exit stress

The study of exit stress can be used to solve the problem of exit breakage in actual machining. Figure 12 shows the contour of the exit stress of the workpiece when grinding the microcrystalline glass. The tool rotates along its axis and moves in the positive direction of the y-axis. The upper edge of the workpiece is the exit during grinding. The

Fig. 11 Curves of the grinding force with rotational speed
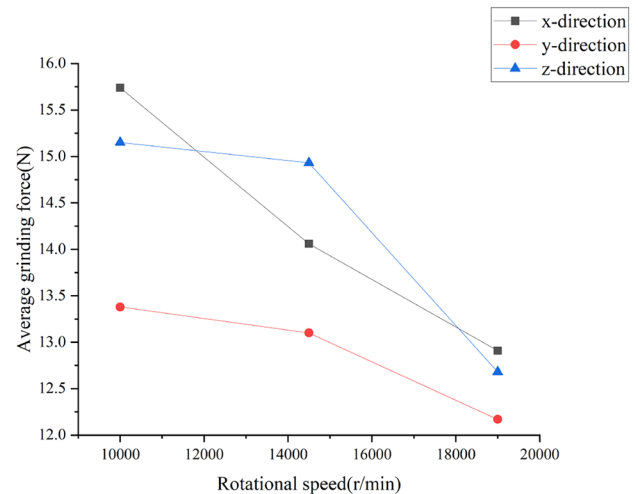
Fig. 12 The stress contour on the workpiece surface
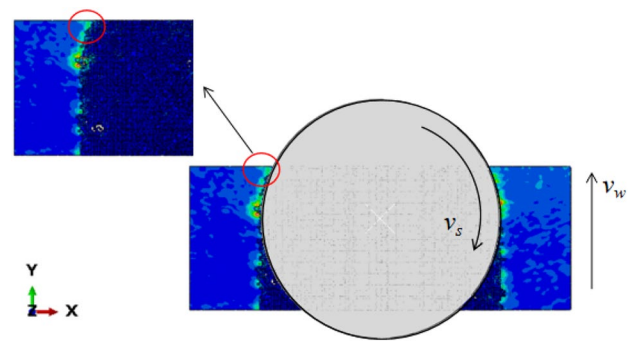
interaction force between the left edge of the tool and the exit areas of the workpiece is the tensile stress, and the interaction force between the right edge of the tool and the exit areas of the workpiece is the compressive stress. The exit breakage of brittle materials during machining is mainly caused by tensile stress, so the left edge of the tool is analyzed.

4.2.1 Effect of feed rates on the exit stress

Figure 13a, b, and c show the stress contour of the workpiece surface at the rotational speed of 10,000 r/min, the grinding depth of 20 μm, and the feed rates of 1000 mm/min, 2000 mm/min, and 3000 mm/min, respectively. As can be seen from Fig. 13, when the feed rate is 1000 mm/min, the stress on the workpiece is mainly distributed at the edge where the workpiece and the tool contact. The maximum stress of the workpiece material is 57.4 MPa, and the stress distribution at the exit is relatively uniform. As the feed rate increases, the maximum stress increases from 87.8 MPa to 110.6 MPa. The reason is that the increase in feed rate raises the maximum depth of a diamond grit that cuts into the workpiece. The workpiece bears more stress as a result of the increased impact between the tool and the workpiece.

4.2.2 Effect of depths on the exit stress

Figure 14a, b, and c are the stress counter images of the workpiece surface at the rotational speed of 10,000 r/min, the feed speed of 3000 mm/min, and the grinding depths of 20 μm, 30 μm, and 40 μm, respectively. As the grinding depth increases, the exit stress of the workpiece material increases from 110.6MPa to 130.1MPa. When the grinding depth is 40 μm, there is a more serious stress concentration at the workpiece exit. The reason is that under the condition of constant feed rate and rotational speed, as the grinding depth increases, the number of diamond grits involved in grinding becomes more. The resistance of the tool and the force in the grinding process becomes larger, resulting in greater stress on the workpiece.
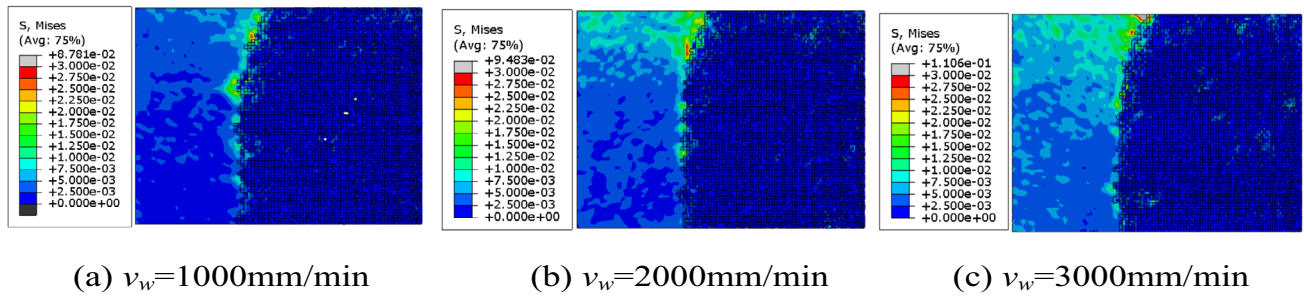
(a) v_w=1000mm/min   (b) v_w=2000mm/min   (c) v_w=3000mm/min

Fig. 13 Effect of feed rates on exit stress

(a) a_p=20μm   (b) a_p=30μm   (c) a_p=40μm
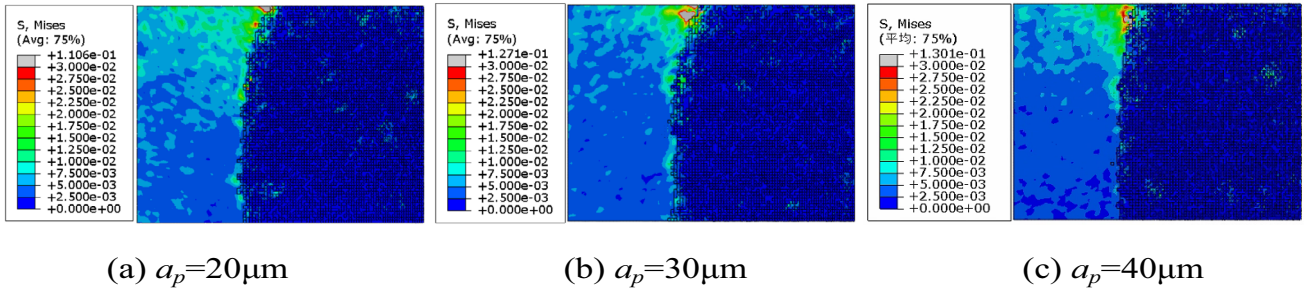
Fig. 14 Effect of depths on exit stress

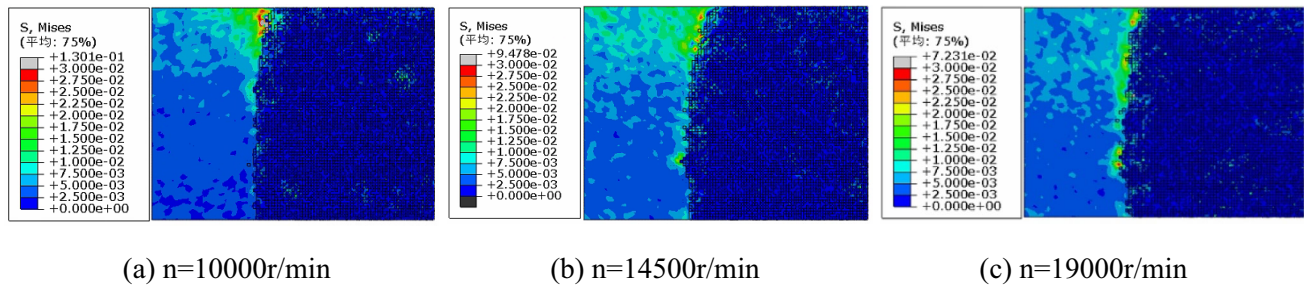(a) n=10000r/min   (b) n=14500r/min   (c) n=19000r/min

Fig. 15 Effect of rotational speeds on exit stress

4.2.3 Effect of rotational speeds on the exit stress

Figure 15a, b, and c show the stress counter diagram of the workpiece surface when the grinding depth is 40 μm, the feed rate is 3000 mm/min, and the rotational speeds is 10,000 r/min, 14,500 r/min, and 19,000 r/min, respectively. As the rotational speed increases, the maximum stress at the exit decreases from 130.1MPa to 72.3MPa, and the stress distribution becomes more uniform. Under the premise of other process parameters unchanged, the rotational speed increases, and the motion distance of a diamond grit each cycle becomes longer. When removing the same material volume, the number of diamond grits involved in grinding becomes more, the maximum depth of a diamond grit each time cuts into the workpiece material decreases, and the interaction force between the tool and the workpiece decreases. Therefore, the stress on the workpiece material is reduced.

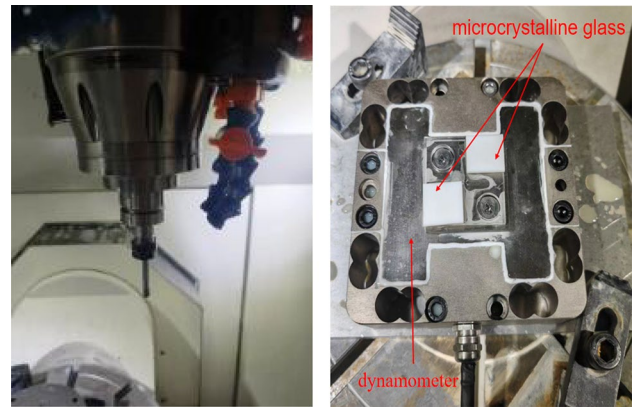**Fig. 16** Microcrystalline glass and tool machining site

Table 4 Performance parameters of Zygo interferometer

Parameter	Value
Model number	Zygo NewView 8300
Vertical resolution	< 0.1 nm
Vertical scanning range	145 μm
Horizontal resolution	0.71 μm
z-axis drive adjustment	0.1 μm
RMS Repeatability	< 0.01 nm
Step measurement repeatability	≤ 0.75%
Step Measurement Accuracy	≤ 0.1%
Table load capacity	3 kg

5 Experimental grinding with ultrasonic vibration-assisted grinding experimental for microcrystalline glass

5.1 Experimental conditions

Figure 16 shows the equipment used in the UVAG experiment. The experiment was carried out on a five-axis machining center. The tool is a 200# electroplated diamond grinding tool with a diameter of 5 mm. To assure the accuracy of the experiment's findings, the workpiece's surface was polished before to the experiment to get rid of surface microcracks left over from the earlier procedure. Coolant injection was used to reduce the grinding temperature. The experiment adopts the three-dimensional force sensor of Viste company, whose model is VC121D. Through VX203 analog signal amplifier, the three-dimensional force will be converted into standard voltage output. Finally, the collected signal is transmitted to the computer through the data acquisition card. After each group of experiments, a Zygo white-light interferometer was used to measure the surface roughness of the machined surface. Its working principle is to obtain the surface morphology of the workpiece by using CSI (continuous scanning interferometry), and the instrument parameters are shown in Table 4. Utilizing an optical image measuring device, the width and thickness of the workpiece's exit breakage were measured. A SEM was used to observe the microscopic surface morphology of the workpiece. The instruments used are shown in Fig. 17a, b, and c.

5.2 Analysis of the experimental results

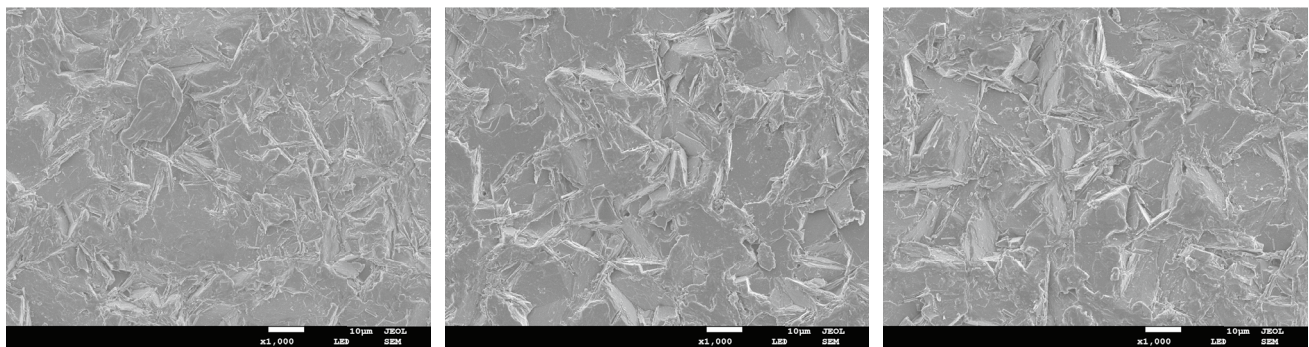### 5.2.1 Effect of process parameters on the surface morphology

Figure 18 shows the surface micromorphology of the group 3–5 by SEM. As can be seen from Fig. 18a, when the grinding depth is 20μm, the material is removed by brittle fracture and plastic deformation simultaneously. There

Fig. 17 Observation Instruments

(a) Zygo NewView 8300   (b) SMV-2010   (c) JSM-7800F

(a) a_p=20μm   (b) a_p =30μm   (c) a_p =40μm

Fig. 18 Surface microscopic morphology after grinding with different grinding depths

are small shallow and cracks as well as a few pits. The surface is relatively smooth. As the grinding depth increases, the microcracks on the workpiece surface increase, because there is more proportion of material removed in a brittle fracture. As can be seen from Fig. 18c, with the increase of grinding depths, the proportion of intact areas on the surface of the machined material is getting smaller. When the grinding depth is 20 μm, the pits on the surface of the workpiece are much shallower than that of 30 μm and 40 μm. And when the grinding depth is increased to 40 μm, there are more pits on the surface of the material and the pits are deeper.

5.2.2 Effect of process parameters on the grinding force

Figures 19, 20 and 21 respectively show the grinding force between the tool and the workpiece during UVAG of microcrystalline glass with different process parameters. The process parameters adopted in machining are the same as those in simulation, as shown in Table 1. It can be seen from the figure that the variation trend of grinding force collected during the experiment is basically the same as that obtained by simulation. The grinding force of z-axis changes more obviously, and the grinding force of x-axis and y-axis remain basically unchanged.

5.2.3 Effect of process parameters on the surface roughness

Figure 22 shows the average value of each group of surface roughness measured by white-light interferometers after machining with the same process parameters as the simulation. Figure 23 shows the surface topography of the workpiece corresponding to the roughness. Groups 1 to 3 show that the surface roughness increases from 1.432μm to 1.672μm as the feed rate increases. When the feed rate is 1000mm/min, the diamond grits at different areas can repeatedly grind the same areas of the workpiece due to the slow feed rate. which plays a role in grinding and cleaning the machined
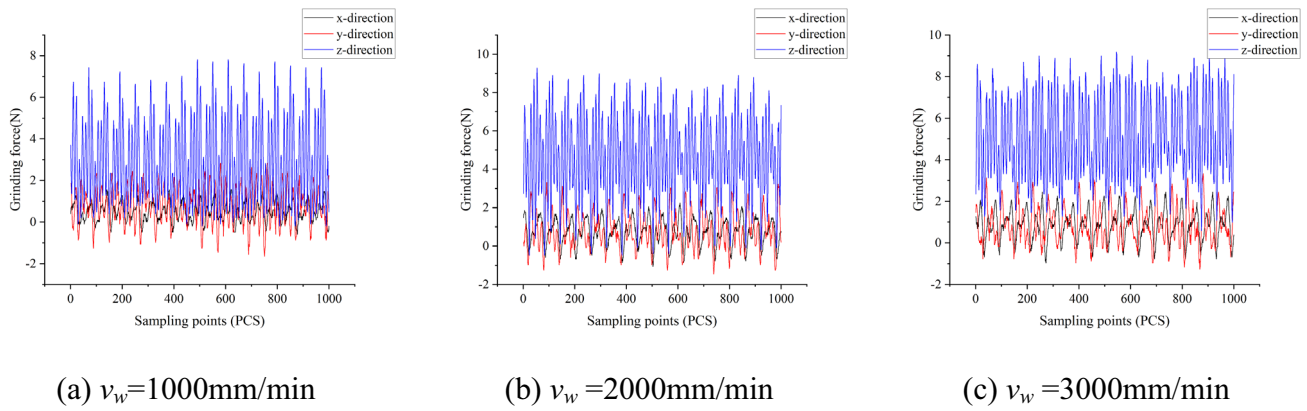
(a) v_w=1000mm/min   (b) v_w =2000mm/min   (c) v_w =3000mm/min

Fig. 19 Grinding force at different feed rates

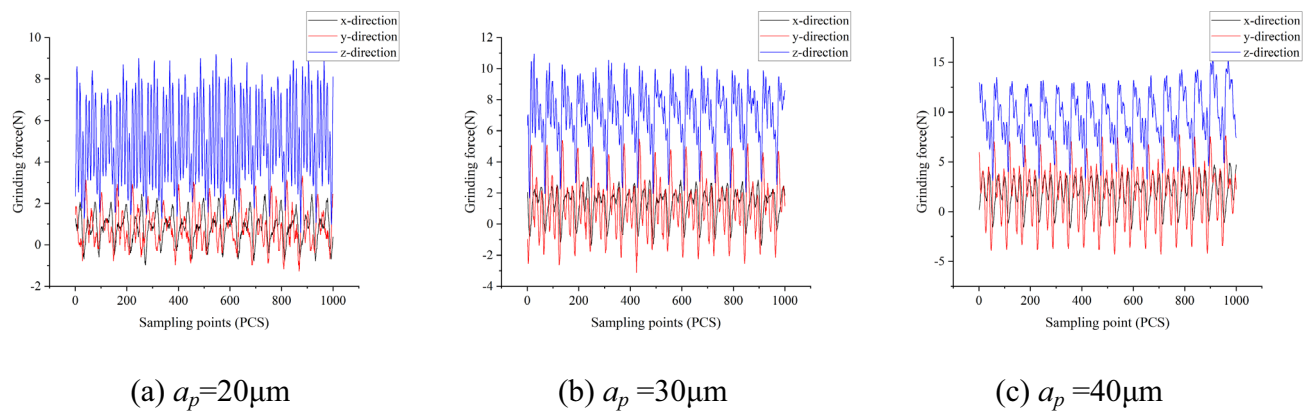(a) a_p=20μm   (b) a_p =30μm   (c) a_p =40μm

Fig. 20 Grinding force at different depths

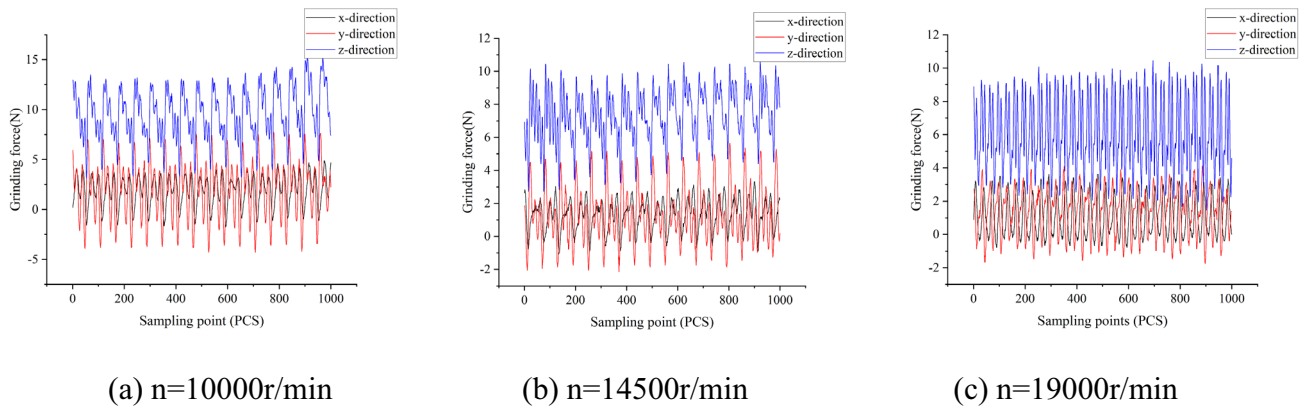(a) n=10000r/min   (b) n=14500r/min   (c) n=19000r/min

Fig. 21 Grinding force at different rotational speeds

surface, so a smooth surface can be obtained. When the feed rate increases, the number of grinding times in the same areas decreases, and the impact between the tool and the workpiece becomes larger, which results in the increasement of grinding force. On this occasion, the workpiece material is mainly removed by brittle fracture, which causes the surface material to crack and fall off, as well as an increase in rough surface roughness. Groups 3 to 5 show that the surface roughness increases from 1.672μm to 1.764μm as the grinding depth increases. As the grinding depth increases, the
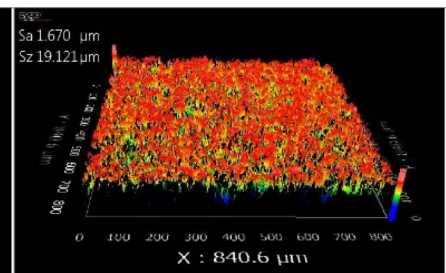
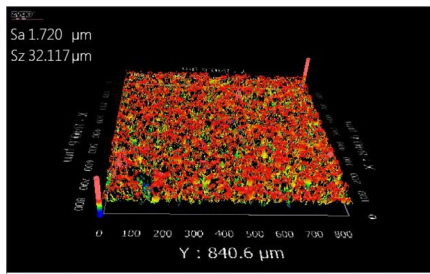**Fig. 22** Average surface roughness of the workpiece after machining
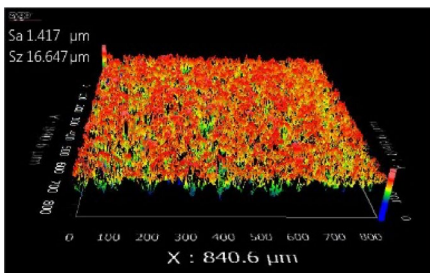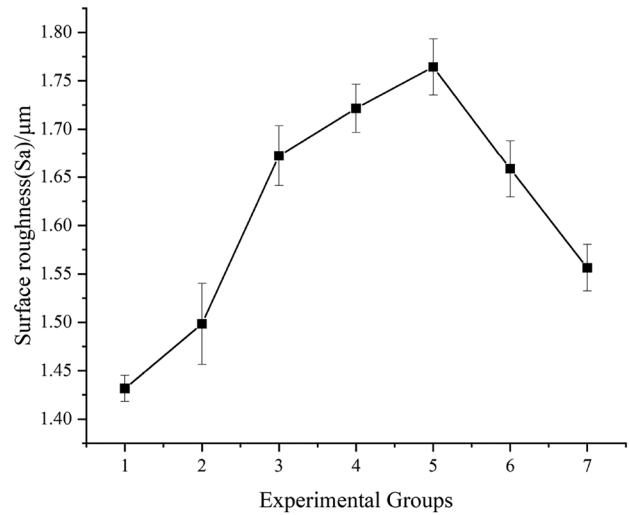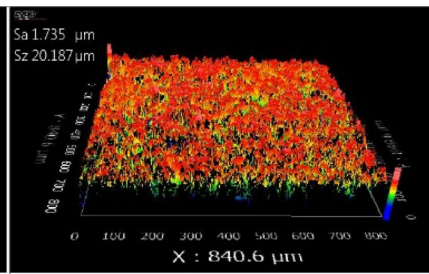

(a)Group 1
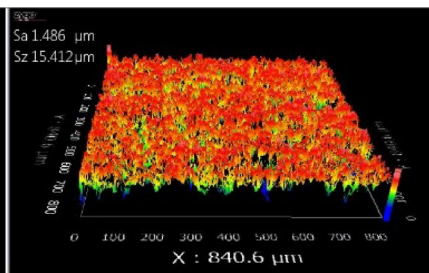
(b)Group 2
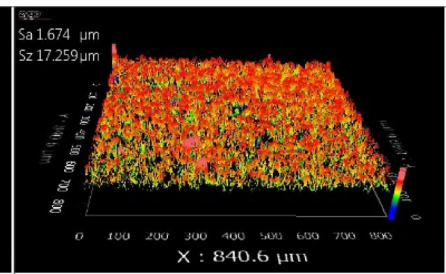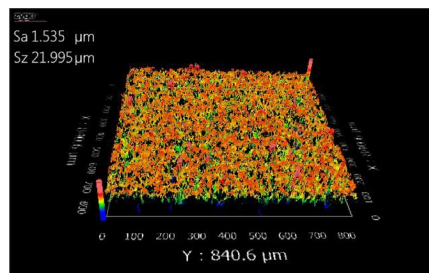
(c)Group 3

(d)Group 4

(e)Group 5

(f)Group 6

(g)Group 7

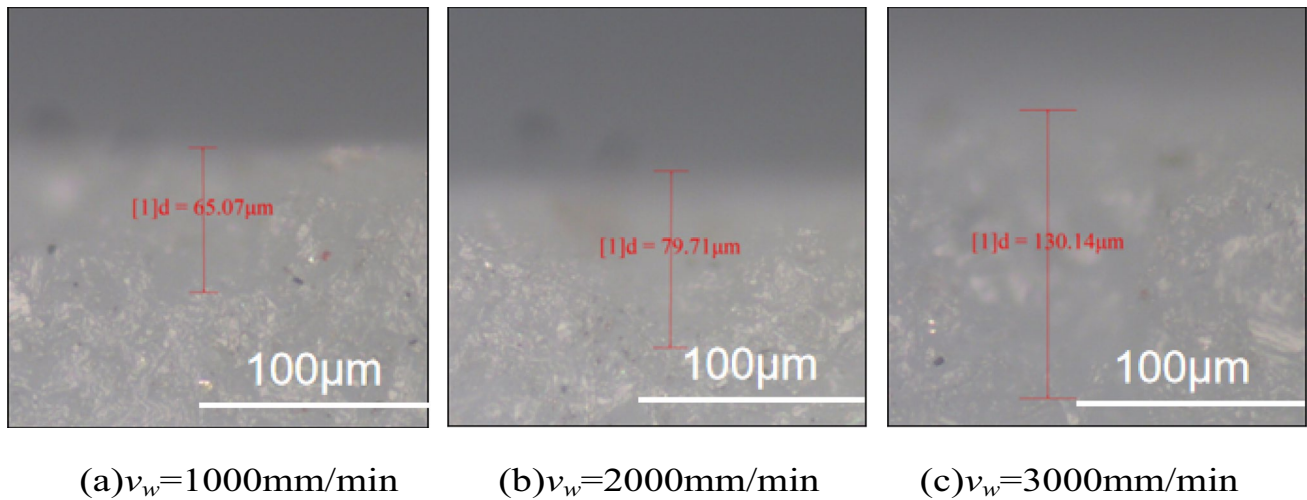**Fig. 23** The surface topography of the workpiece after machining

(a)v_w=1000mm/min   (b)v_w=2000mm/min   (c)v_w=3000mm/min

Fig. 24 The thickness of exit breakage under different feed rates

(a) Average width of the exit breakage   (b) Average thickness of the exit breakage
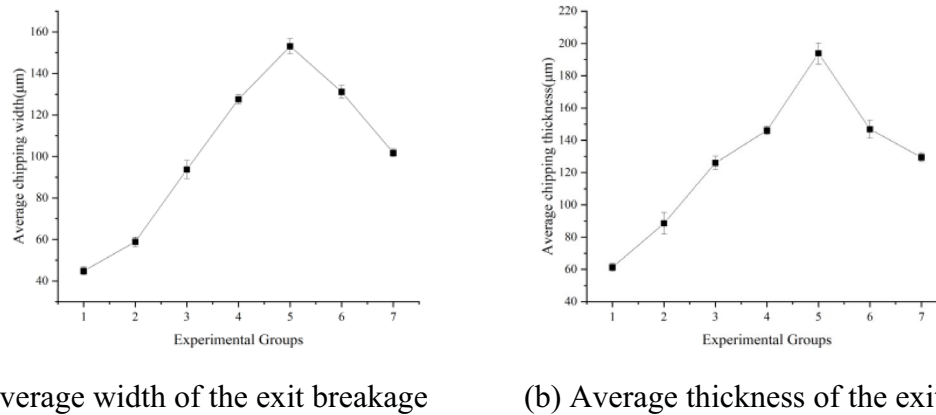
Fig. 25 The width and thickness of the exit breakage after machining

actual cutting thickness of diamond grits increases, and the volume of material removal in a cycle increases. The deeper the grinding depth is, the more difficult the chips are removed. Many chips are adhered to the tool and the number of effective grits in contact with the workpiece material is reduced. Therefore, both surface cracks and surface roughness increase. Groups 5 to 7 show that the surface roughness decreases from 1.764μm to 1.556μm as the rotational speed increases. The reason is that the increase in rotational speed increases the number of diamond grits scratching the machined surface and reduces the grinding thickness when the diamond grits cut into the workpiece at a single time. More diamond grits are involved in grinding at the same position on the workpiece, and the surface roughness of the workpiece is reduced after machining.

5.2.4 Effect of process parameters on the exit breakage

Figure 24a, b, and c show the exit breakage thickness of the workpiece after grinding at different feed rates. Figure 25 shows the curves of the average width and thickness of the exit breakage during grinding for each group. As the feed rate increases, the width and thickness of the exit breakage increase from 45.01μm to 93.27μm, and from 59.65μm to 120.38μm, respectively. A higher feed rate causes the workpiece's cutting width to rise in a horizontal direction, which results in a larger exit breakage. It is concluded that a higher feed rate leads to a higher stress concentration at the edges of the workpiece and leads to exit breakage, which validates the reliability of the simulation model. As the grinding depth increases, the average exit breakage width increases from 93.27μm to 154μm, and the average exit breakage

thickness increases from 120.38μm to 191.42μm. This is because the increase in grinding depth increases the grinding force of the tool on the workpiece, the stress at the exit of the workpiece increases and the stress is concentrated. The material is mainly removed by brittle fracture. Therefore, the width and thickness of the exit breakage are increased. As the rotational speed increases, the width of the exit breakage decreases from 154μm to 103.2μm, and the thickness of the exit breakage decreases from 191.42μm to 130.14μm. This is because the increase in rotational speed increases the number of diamond grits that scratch the workpiece surface. The grinding width of the diamond grits is reduced when the workpiece is cut into the workpiece in a cycle, and the workpiece is machined with a lower grinding force and stress, reducing the width and thickness of the exit breakage.

6 Comparative analyses with previous work

In the current work, the effects of process parameters on grinding force, exit stress, surface morphology and exit breakage are studied by combining simulation and experiment. As can be seen from the literature, Zhang et al. [10] proposed a new method for calculating grinding force on the basis of establishing the mathematical model of grinding force, and verified the accuracy of the theoretical derivation through numerical calculation and comparative experiment. The results show that the grinding force increases with the increase of grinding depth and feed rate, and decreases with the increase of rotational speed, which is consistent with the research results in this paper. Xiong et al. [17] obtained similar conclusions by conducting UVAG experiments on SiCf/SiC CMC to evaluate the effect of process parameters on grinding force. In addition, Tong et al. [18] made a comparative analysis of ultrasonic vibration-assisted grinding and conventional grinding, and found that ultrasonic vibration can significantly improve the phenomenon of edge break damage and surface quality of optical glass exit. Peng et al. [19] used ABAQUS simulation software to study the formation mechanism and stress distribution of edge defects in the process of UVAG, and conducted comparative analysis through experiments. According to the results, the exit position edge defects are the most serious. Furthermore, it is discovered that better edge quality can be obtained within a certain ranges of ultrasonic amplitude.

7 Conclusion

In this paper, an ellipsoidal erosion model based on the motion characteristics of a single diamond grit is proposed to solve the problems such as exit breakage and surface micro-cracks in microcrystalline glass machining. A simulation model of ultrasonic vibration-assisted grinding of microcrystalline glass is established using the finite element method, and the effect of feed rate, grinding depth, and rotational speed on the grinding force as well as the exit stress distribution on the workpiece were investigated. Using a five-axis CNC machine, microcrystalline glass grinding experiments are conducted. Surface morphology, surface roughness, and exit breakage sizes of the glass are measured and observed. The conclusions are as follows:

(1) The grinding force and stress between the tool and the workpiece show a tendency of gradual rise with increasing feed rate and grinding depth. As the rotational speed increases, the grinding force and stress decrease gradually.

(2) As the feed rate increases, the maximum stress at the workpiece exit increases from 87.8MPa to 110.6MPa. As the grinding depth increases, the maximum stress at the workpiece exit increases from 110.6MPa to 130.1MPa. As the rotational speed increases, the maximum stress at the workpiece exit decreases from 130.1MPa to 72.3MPa.

(3) As the grinding depth increases, the proportion of brittle fracture removal on the workpiece surface increased, while the proportion of plastic flow decreased.

In the present study, we studied the effect of process parameters on surface roughness and exit breakage of the workpiece with actual production conditions. The parameters used in this study are for production and have important theoretical significance for production practice. Ultrasonic vibration-assisted grinding is a complex machining system, which involves the comprehensive action of many factors and parameters, including ultrasonic vibration frequency, amplitude, tool material, tool geometry parameters, etc. Therefore, in the follow-up research, we will continue to explore the impact of tool material, tool geometric parameters and other factors on surface roughness and exit breakage.

Declarations

Competing interests The authors declare no competing interests.

References

1. Zhang H, Du Y, Yang X, et al. Influence of rare earth ions on metal ions distribution and corrosion behavior of tailing-derived glass-ceramics. J Non-Cryst Solids. 2018;482:105–15. https://doi.org/10.1016/j.jnoncrysol.2017.12.028.
2. Zhang Z, Yao P, Li X, et al. Grinding performance and tribological behavior in solid lubricant assisted grinding of glass-ceramics. J Manuf Process. 2020;51:31–43. https://doi.org/10.1016/j.jmapro.2020.01.020.
3. Feucht F, Ketelaer J, Wolff A, et al. Latest machining technologies of hard-to-cut materials by ultrasonic machine tool. Procedia CIRP. 2014;14:148–52. https://doi.org/10.1016/j.procir.2014.03.040.
4. Sun YZ, Zhang J, Liu HT, et al. Experimental research on ultrasonic torsional vibration-assisted grinding of hard and brittle materials. Key Eng Mater. 2014;579–580:101–4. https://doi.org/10.4028/www.scientific.net/KEM.579-580.101.
5. Ding K, Fu Y, Su H, et al. Experimental studies on matching performance of grinding and vibration parameters in ultrasonic assisted grinding of SiC ceramics. Int J Adv Manuf Technol. 2017. https://doi.org/10.1007/s00170-016-8977-6.
6. Li C, Zhang F, Meng B, et al. Material removal mechanism and grinding force modelling of ultrasonic vibration assisted grinding for SiC ceramics. Ceram Int. 2017;43(3):2981–93. https://doi.org/10.1016/j.ceramint.2016.11.066.
7. Baraheni M, Amini S. Investigation on rotary ultrasonic assisted end grinding of silicon nitride ceramics. SN Appl Sci. 2019;1(12):1560. https://doi.org/10.1007/s42452-019-1594-x.
8. Wang D, Fan H, Xu D, et al. Research on grinding force of ultrasonic vibration-assisted grinding of C/SiC composite materials. Appl Sci. 2022. https://doi.org/10.3390/app122010352.
9. Chen Y, Hu Z, Yu Y, et al. Processing and machining mechanism of ultrasonic vibration-assisted grinding on sapphire. Mater Sci Semicond Process. 2022. https://doi.org/10.1016/j.mssp.2022.106470.
10. Zhang X, Yang L, Wang Y, et al. Mechanism study on ultrasonic vibration assisted face grinding of Hard and brittle materials. J Manuf Process. 2020;50:520–7. https://doi.org/10.1016/j.jmapro.2020.01.003.
11. Guo B, Zhao Q. Ultrasonic vibration assisted grinding of hard and brittle linear micro-structured surfaces. Precis Eng. 2017;48:98–106. https://doi.org/10.1016/j.precisioneng.2016.11.009.
12. Yang Z, Zhu L, Zhang G, et al. Review of ultrasonic vibration-assisted machining in advanced materials. Int J Mach Tools Manuf. 2020;156:103594. https://doi.org/10.1016/j.ijmachtools.2020.103594.
13. Yang Z, Zou P, Zhou L, et al. Research on the machining mechanism of AISI 304 ultrasonic vibration assisted grinding. Appl Acoust. 2023;214:109712. https://doi.org/10.1016/j.apacoust.2023.109712.
14. Brehl DE, Dow TA. Review of vibration-assisted machining. Precis Eng. 2008;32(3):153–72. https://doi.org/10.1016/j.precisioneng.2007.08.003.
15. Yao W, Chu Q, Lyu B, et al. Modeling of material removal based on multi-scale contact in cylindrical polishing. Int J Mech Sci. 2022;223:107287. https://doi.org/10.1016/j.ijmecsci.2022.107287.
16. Yao W, Lyu B, Zhang T, et al. Effect of elastohydrodynamic characteristics on surface roughness in cylindrical shear thickening polishing process. Wear. 2023;530–531:205026. https://doi.org/10.1016/j.wear.2023.205026.
17. Xiong Y, Wang W, Jiang R, et al. Feasibility and tool performance of ultrasonic vibration-assisted milling-grinding SiCf/SiC ceramic matrix composite. J Mater Res Technol. 2022;19:3018–33. https://doi.org/10.1016/j.jmrt.2022.06.063.
18. Tong J, Yang S, Ye Y, et al. Edge breakage mechanism of optical glass surface in ultrasonic vibration-assisted milling. Int J Adv Manuf Technol. 2023. https://doi.org/10.1007/s00170-023-11093-x.
19. Peng P, Xiang D, Lei X, et al. Study on the edge defects of high volume fraction 70% SiCp/Al composites in ultrasonic-assisted milling. Int J Adv Manuf Technol. 2022;122(1):485–98. https://doi.org/10.1007/s00170-021-08586-y.

Discover